Supporting Information

Effects of Mg and Sn elements on the microstructure and properties of the Al-Zn-In-Ga sacrificial anode

WU Qi-yue(吴琦月)[1,2], LIU Xing-ling(刘杏灵)[1], XIE Chao-ying(谢朝颖)[1], TANG Wen-tao(唐文涛)[1], WANG Ri-chu(王日初)[1], PENG Chao-qun(彭超群)[1], FENG Yan(冯艳)[1,2]

1.School of Materials Science and Engineering, Central South University, Changsha 410083, China
2.State Key Laboratory of Powder Metallurgy, Central South University, Changsha 410083, China

1. Materials and methodsThe polishing, cleaning, and sanitization processes in preparation of coupons

Before microstructural observation and electrochemical performance testing, the alloy samples were carefully prepared: first, they were wet-ground using 400#, 800#, 1000#, and 1500# sandpaper, followed by fine grinding with 800# and 1500# metallographic sandpaper, and finally polished with silicon carbide paste. Before the metallographic testing, the samples were etched using Keller's reagent for 15 seconds. Before the TEM test, the samples were mechanically ground to about 50 μm and then cut into circular slices of 3 mm in diameter. The double-jet thinning voltage was set to 20 V, the temperature was -30 °C and the dual injection solution was 30% HNO3 and 70% CH3OH.

1.2. Sample pretreatment process for corrosion behaviour observation

After 7 days of corrosion, the samples were removed and immersed in a solution containing 68% HNO_3. They were then ultrasonically cleaned for 10 minutes to remove surface corrosion products. Subsequently, the samples were rinsed with distilled water and ultrasonically cleaned, then thoroughly rinsed with anhydrous ethanol solution. For samples used to calculate the self-corrosion rate, they were dried in a 50°C oven for 1 hour before corrosion and after removing corrosion products, then weighed after moisture removal.

1.3. The electrochemical measurements parameters

Open-circuit potential (OCP) was monitored for 300 seconds to ensure stability. Potential-driven polarization measurements were conducted within a voltage range of -1.6 to -0.5 V relative to the SCE, with a potential scan rate of 5 mV/s. Polarization curves were fitted using CView software. For EIS characterization, frequency scans covered a broad spectrum from 10^5 Hz to 10^{-2} Hz, and the obtained spectra were subsequently modelled and interpreted using ZSimpWin analysis software.

1.4. Anode current efficiency test setup

The current density settings for each experimental stage are detailed in Table .

Table S1 Current density setting based on anode working area

Time (h)	Current density (mA cm^{-2})
0 ~ 24	1.5
> 24 ~ 48	0.4
> 48 ~ 72	4.0
> 72 ~ 96	1.5

2. Materials and methodsMicrostructure supplement experiment and analysis

The grain sizes of the three alloys were quantitatively analyzed, and the resulting size distribution diagrams are presented in **Figure S1**. Adding Mg and Sn elements reduces the peak grain size from 375 μm to 175 μm. This result indicates that the Mg and Sn elements lead to grain size refinement in Al-Zn-In-Ga alloy.

To further determine the composition of the Mg-Sn-rich phases in Al-Zn-In-Ga-Mg-Sn alloy, the second phase was observed by TEM. **Figure S2** shows the TEM bright-field image and the corresponding selected area electron diffraction (SAED) pattern of the Al-Zn-In-Ga-Mg-Sn alloy, where Fig.5(a) shows the bright-field image and Fig.5(b, c) shows the diffraction patterns corresponding to the different crystallographic band axes of the phase. As shown in Fig.5(a), a larger Mg-Sn-rich phase can be observed. As shown in Fig.5(b), the crystal spacings of (113), $(4\bar{2}3)$ and $(3\bar{3}0)$ in the Mg-Sn-rich phase diffraction pattern along the $[\bar{3},\bar{3},2]$ band axis are 0.378, 0.271 and 0.387 nm, respectively. It is reported that the cellular parameters of Mg_9Sn_5 are a=1.324 nm, b=1.324 nm, c=1.334 nm, α=β=90°, γ=120°[1]. The corresponding crystallite spacings were calculated to be 0.3691 nm, 0.2655 nm, and 0.3822 nm, with an error of less than 5% between the measured and theoretical values. The measured angle between the (113) and $(4\bar{2}3)$ directions is 44.41°, and the measured angle between the (113) and $(3\bar{3}0)$ directions is 90.16°, which is consistent with the corresponding theoretical crystallographic interstitial angles of 44.00° and 90° in Mg_9Sn_5. Similarly, as shown in Fig.5(b), the crystal spacing of $(2\bar{1}\bar{3})$, $(\bar{3}30)$, and $(\bar{1}2\bar{3})$ in the Mg-Sn-rich phase pattern along the [3,3,1] band axis are 0.376, 0.387, and 0.376 nm, respectively. The corresponding crystallographic plane spacings are calculated from the cellular parameters of Mg_9Sn_5 to 0.3691 nm, 0.3822 nm and 0.3691 nm, and the error between the measured and theoretical values is less than 5%. The measured angles between the $(2\bar{1}\bar{3})$ and $(\bar{1}2\bar{3})$ directions are 58.03° and between the $(2\bar{1}\bar{3})$ and $(\bar{3}30)$ directions are 119.01°, which are in accordance with the corresponding theoretical crystallographic interfacial angles of 57.75° and 118.87°. In summary, the second phase in Al-Zn-In-Ga-Mg-Sn alloy is Mg_9Sn_5.

Figure S3 shows the EDS results of the second phase transmission image. The second phase is mainly enriched with Mg and Sn elements, and there is a small amount of In element deposition.

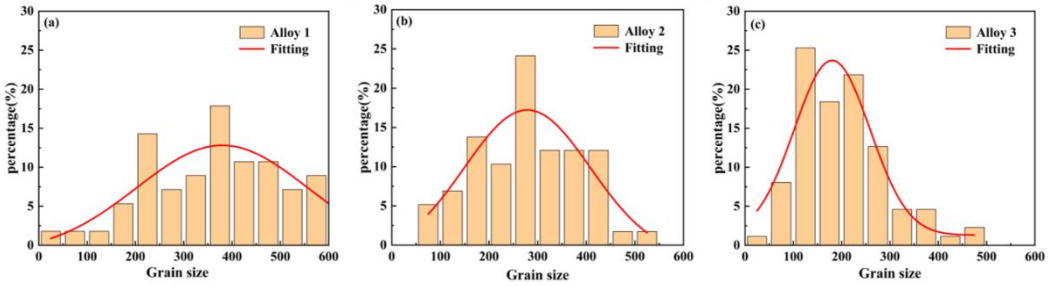

Figure S1 Grain size distribution of Al-Zn-In-Ga system sacrificial anodes (a)Al-5.5Zn-0.03In-0.03Ga, (b)Al-5.5Zn-0.03In-0.03Ga-1Mg, (c)Al-5.5Zn-0.03In-0.03Ga-1Mg-0.05Sn

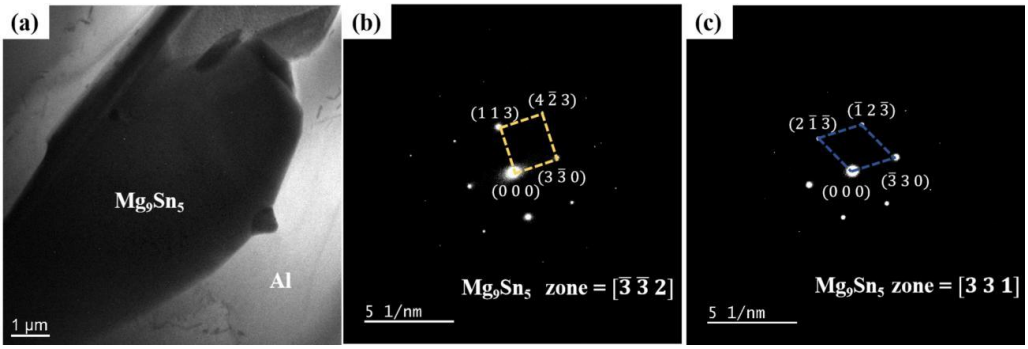

Figure S2 The TEM image of second phase in Al-Zn-In-Ga-Mg-Sn alloy (a)TEM bright field micrograph, (b, c)SAED patterns of precipitate along different directions electron beam incident directions

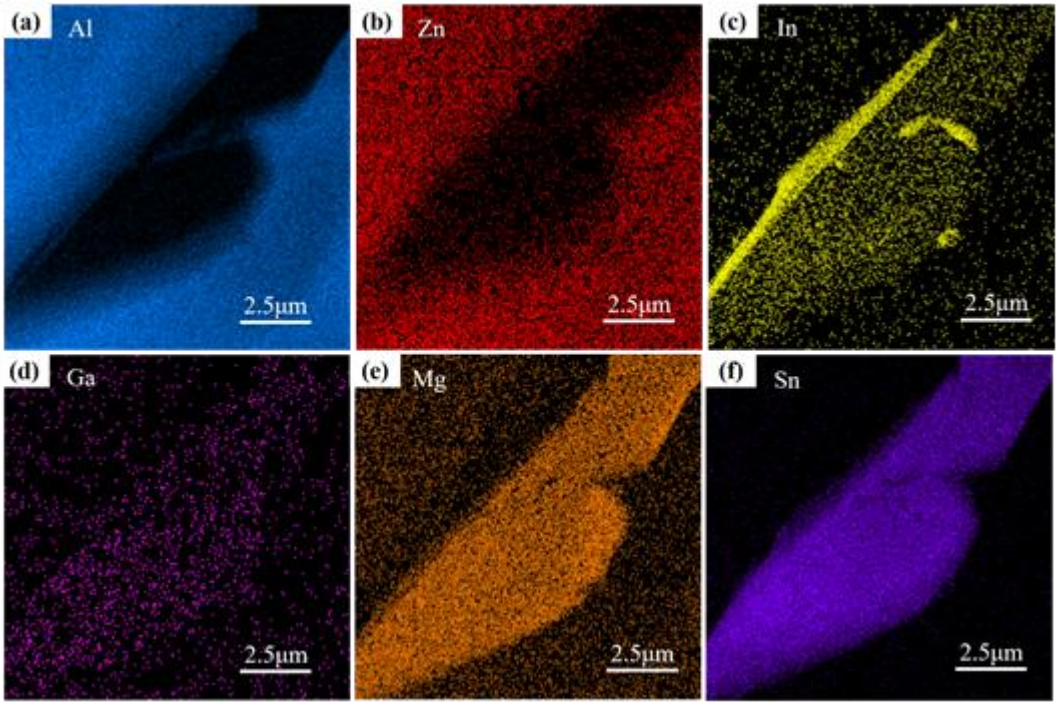

Figure S3 EDS analysis results of the second-phase TEM image

2.2. Warburg impedance analysis

The Warburg impedance in this study can be attributed to the diffusion resistance of solution ions [2]. As the corrosion process progresses, corrosion products continuously accumulate on the electrode surface, forming a porous and uneven corrosion product film. This film allows solution ions to reach the substrate through defects or pores, thereby continuing the corrosion process. In this case, the film is unable to effectively block the current, so the resistance of the corrosion-resistant film is not significant. Therefore, the low-frequency electrochemical response of the system is primarily dominated by the diffusion of solution ions and corrosion products. Consequently, Warburg impedance is observed in the low-frequency region of the electrochemical impedance spectra of the three alloys.

2.3. XPS analysis of corrosion products

XPS spectra of the corrosion products are shown in **Figure S4**. The C peaks are from CO_2 in solution and air, and the Al, O, Zn, and Mg peaks are from the alloys and the corrosion products. The binding energy was corrected for charge effects concerning the C 1s peak at 284.80 eV. **Figure S4** (a) shows the XPS total spectra of three Al-Zn-In-Ga alloys after corrosion 7d. **Figure S4** (b - e) shows the high-resolution spectra of Al 2p, Zn 2p, Mg 1s, and O 1s after 7 days of corrosion. The peaks of Al 2p are all located near the literature value (74.4 eV), which is derived from Al (III) [3]. The two spin-orbit split peaks of Zn 2p, 2p1 (1044.8 eV) and 2p3 (1021.8 eV), have a binding energy difference of 23 eV, corresponding to Zn(II) [4]. All peaks of Mg 1s are located near 1303.7 eV, corresponding to Mg(II) [5, 6]. The O 1s peaks of the three alloys are all located near the literature value (531.8 eV), which originates from OH^- [5]. These results indicate that the primary corrosion products of the three alloys are $Al(OH)_3$ and $Zn(OH)_2$. Additionally, the corrosion products of the Al-Zn-In-Ga-Mg and Al-Zn-In-Ga-Mg-Sn alloys contain trace amounts of $Mg(OH)_2$.

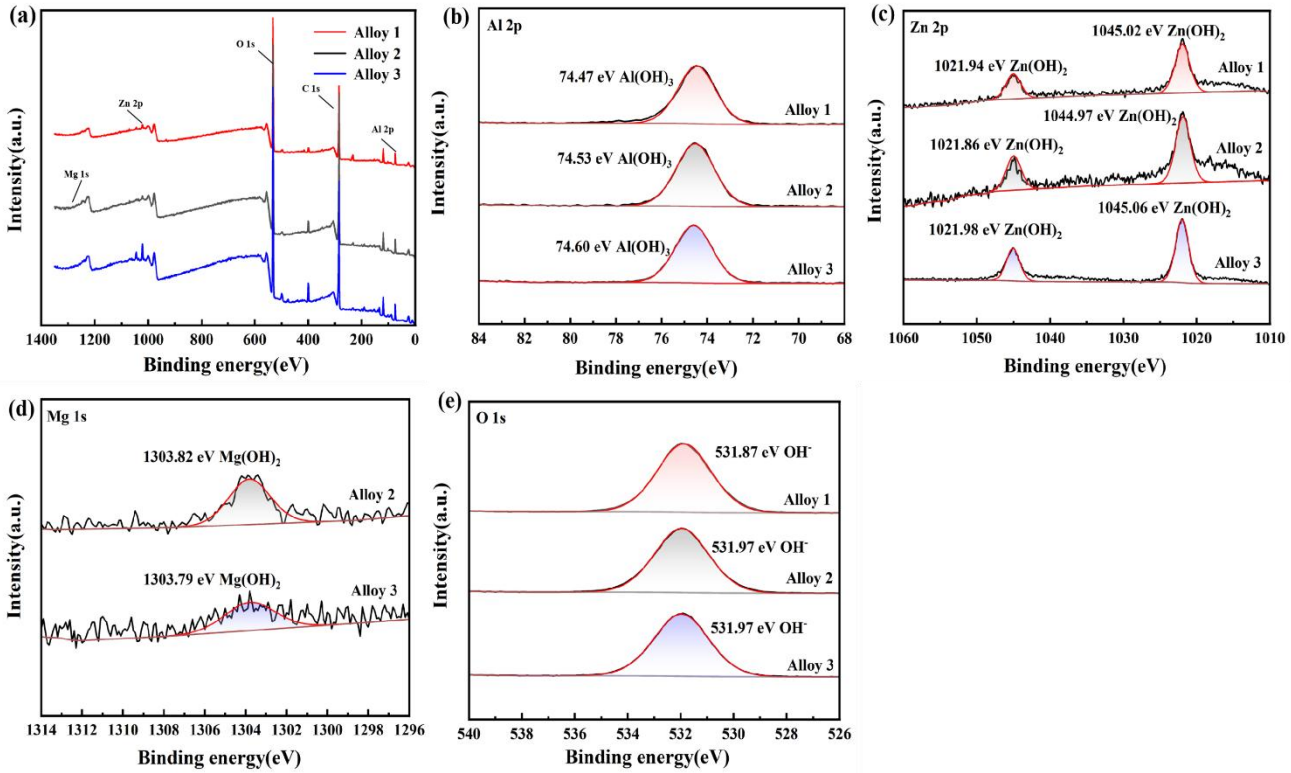

Figure S4 XPS spectra of three Al-Zn-In-Ga alloys after corrosion in 3.5% NaCl solution for 7 d (a)survey spectra, (b)Al 2p spectrum, (c)Zn 2p spectrum, (d)Mg 1s spectrum, (e)O 1s spectrum.

References

[1] FONG A. Y., XU H., PAGE K., et al. Synthesis and structural characterization of dense polycrystalline Mg9Sn5, a metastable Mg-Sn phase[J]. Journal of Alloys and Compounds, 2014, 616: 333-339. DOI: 10.1016/j.jallcom.2014.07.122

[2] JIANG X G, SONG J W, WANG X B, et al. Improved 3D porous structures of Ni electrodes prepared by high-pressure cold spray and post annealing for water splitting[J]. International Journal of Hydrogen Energy, 2022, 47(27): 13226-13239. DOI: 10.1016/j.ijhydene.2022.02.088

[3] PENG Can, LIU Yu-wei, GUO Ming-xiao, et al. Corrosion and pitting behavior of pure aluminum 1060 exposed to Nansha Islands tropical marine atmosphere[J]. Transactions of Nonferrous Metals Society of China, 2022, 32(2): 448-460. DOI: 10.1016/s1003-6326(22)65806-0

[4] WANG Yan-qi, KONG Gang, CHE Chun-shan. Corrosion Behavior of Zn-Al, Zn-Mg, and Zn-Mg-Al Coatings in Simulated Concrete Pore Solution[J]. Corrosion, 2018, 75(2): 203-209. DOI: 10.5006/3029

[5] WANG Jia-ming, YANG Hao-dong, DU Min, et al. Corrosion Mechanism of 5083 Aluminum Alloy in Seawater Containing Phosphate[J]. Journal of Ocean University of China, 2021, 20(2): 372-382. DOI: 10.1007/s11802-021-4545-2

[6] CHEN Yu-qiang, WU Hai-liang, WANG Xiang-dong, et al. Corrosion Mechanism and the Effect of Corrosion Time on Mechanical Behavior of 5083/6005A Welded Joints in a NaCl and NaHSO3 Mixed Solution[J]. Crystals, 2022, 12(8). DOI: 10.3390/cryst12081150